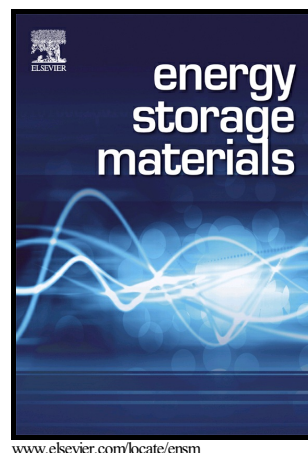


H-Nb<sub>2</sub>O<sub>5</sub> Wired by Tetragonal Tungsten Bronze  
Related Domains as High-Rate Anode for Li-ion  
Batteries

Dunping Cao, Jincang Zhang, Chilin Li



PII: S2405-8297(17)30338-0  
DOI: <https://doi.org/10.1016/j.ensm.2017.10.005>  
Reference: ENSM227

To appear in: *Energy Storage Materials*

Received date: 2 August 2017  
Revised date: 20 September 2017  
Accepted date: 9 October 2017

Cite this article as: Dunping Cao, Jincang Zhang and Chilin Li, H-Nb<sub>2</sub>O<sub>5</sub> Wired by Tetragonal Tungsten Bronze Related Domains as High-Rate Anode for Li-ion Batteries, *Energy Storage Materials*, <https://doi.org/10.1016/j.ensm.2017.10.005>

This is a PDF file of an unedited manuscript that has been accepted for publication. As a service to our customers we are providing this early version of the manuscript. The manuscript will undergo copyediting, typesetting, and review of the resulting galley proof before it is published in its final citable form. Please note that during the production process errors may be discovered which could affect the content, and all legal disclaimers that apply to the journal pertain.

# H-Nb<sub>2</sub>O<sub>5</sub> Wired by Tetragonal Tungsten Bronze Related Domains as High-Rate Anode for Li-ion Batteries

Dunping Cao,<sup>a,b</sup> Jincang Zhang,<sup>b,\*</sup> and Chilin Li<sup>a,\*</sup>

<sup>a</sup> State Key Laboratory of High Performance Ceramics and Superfine Microstructure, Shanghai Institute of Ceramics, Chinese Academy of Sciences, Shanghai 200050, China. Email: chilinli@mail.sic.ac.cn

<sup>b</sup> Materials Genome Institute & Department of Physics, Shanghai University, Shanghai 200444, China. Email: jczhang@shu.edu.cn

**Abstract:** Nb-based oxide is a promising candidate of high-rate anodes to develop high power Li-ion batteries and Li-ion capacitors. Compared with metastable bronze phase T-Nb<sub>2</sub>O<sub>5</sub> with remarkable intercalation pseudocapacitance, commercially available high-temperature phase H-Nb<sub>2</sub>O<sub>5</sub> is still of low-rate performance in view of the absence of Nb-O pentagonal bipyramids, an important moieties to construct desired “room-and-pillar” framework with open interconnected channels. Here we introduce a small fraction of tetragonal tungsten bronze (TTB) related KNb<sub>6</sub>O<sub>15</sub>F as conductive wires into H-Nb<sub>2</sub>O<sub>5</sub> by simply doping KF. These KNb<sub>6</sub>O<sub>15</sub>F nano-sticks with NbO<sub>5</sub>F<sub>2</sub> pentagonal bipyramids are electrochemically robust and of high rate performance themselves, contributing significant gain on capacity retention, rate endurance and capacitance effect for H-Nb<sub>2</sub>O<sub>5</sub>. The resultant rate performance is extraordinary with reversible capacities of 120, 100 and 80 mAh/g at 5C, 10C and 20C respectively. In-situ wiring by phase segregation within a compact space based on correlated phase diagram appears to be a good solution to boosting of electron (or ion) flux especially when the wires are electroactive in the similar voltage zone.

**Keywords:** Nb<sub>2</sub>O<sub>5</sub>, Intercalation anode, Oxyfluoride, Wiring network, Li-ion batteries

## Introduction

Li-ion batteries (LIBs) have been widely used in portable electronics, and are expected to be a promising power source in electric vehicles due to their potential of superior energy/power density performance compared to traditional secondary batteries. In order to further improve the power density (or pseudocapacitance contribution), research enthusiasm has focused on novel electrode materials with mineral-inspired open framework structure and defect-rich nanoparticles.<sup>1-4</sup> At the anode side, Ti-based oxides have been widely accepted as high-rate intercalation materials, e.g.  $\text{TiO}_2(\text{B})$  and  $\text{Li}_4\text{Ti}_5\text{O}_{12}$ .<sup>5,6</sup> However the activation of their high power performance and pseudocapacitance effect still requires well-designed electronic wiring and nano-engineering on active species. Compared to  $\text{Li}_4\text{Ti}_5\text{O}_{12}$ ,  $\text{Nb}_2\text{O}_5$  has a higher theoretical capacity (200 mAh/g vs. 175 mAh/g for  $\text{Li}_4\text{Ti}_5\text{O}_{12}$ ) and comparable voltage plateau (~1.7 V vs. ~1.6 V for  $\text{Li}_4\text{Ti}_5\text{O}_{12}$ ).<sup>7</sup>  $\text{Nb}^{5+}$  has a larger ionic radius (64 pm) than that (60.5 pm) of  $\text{Ti}^{4+}$  and therefore its substitution of Ti can result in lattice expansion, extension of solid-solution reaction zone and potentially better rate performance.<sup>8</sup> Indeed, recently Dunn et al. discovered that orthorhombic  $\text{Nb}_2\text{O}_5$  (low temperature phase, denoted as T- $\text{Nb}_2\text{O}_5$ ) in a form of mesoporous and nanocrystal films displays high rate electrochemical energy storage (higher capacity than  $\text{Li}_4\text{Ti}_5\text{O}_{12}$  at higher rate) and ascribed it to a new reaction mechanism termed intercalation pseudocapacitance.<sup>9-11</sup> This kind of pseudocapacitance is thought to be intrinsic and activated by open crystalline network with interconnected (two-dimensional) channels and low energy barrier migration sites, different from the extrinsic pseudocapacitance caused by surface redox reaction scaling with grain size.<sup>12</sup> Further, Grey et al. disclosed that high-rate (de)intercalation of metastable T- $\text{Nb}_2\text{O}_5$  can also be achieved even without intentional nanostructuring.<sup>13</sup> Although monoclinic  $\text{Nb}_2\text{O}_5$  (thermodynamically most stable high-temperature phase, denoted as H- $\text{Nb}_2\text{O}_5$ ) displays larger initial capacity than T- $\text{Nb}_2\text{O}_5$ , its capacity retention and rate performance are remarkably inferior to T- $\text{Nb}_2\text{O}_5$  where the unique “room-and-pillar”  $\text{NbO}_6/\text{NbO}_7$  framework is thought to be responsible for the more stable and faster accommodation of Li atoms. The rate performance of other  $\text{Nb}_2\text{O}_5$  polymorphs (e.g. B- $\text{Nb}_2\text{O}_5$ , TT- $\text{Nb}_2\text{O}_5$ ) lies between those of T- $\text{Nb}_2\text{O}_5$  and H- $\text{Nb}_2\text{O}_5$ .<sup>13</sup>

Therefore previous research interests mainly focused on T-Nb<sub>2</sub>O<sub>5</sub>, including its nano-morphology and nano-composite strategies.<sup>14-18</sup> How to upgrade the electrochemical performance of commercially available H-Nb<sub>2</sub>O<sub>5</sub> is still a big challenge so far.

Nb<sub>2</sub>O<sub>5</sub> is an electronic insulator, and its bandgap ranges from 3.2 to 4 eV dependent on oxygen stoichiometry.<sup>19</sup> Although marginal lithiation can trigger a quick transition to electronic conductor with conductivity upgrade by four orders of magnitude, the capacity performance of Nb<sub>2</sub>O<sub>5</sub> especially under high-rate charging is still limited. Dual surface decoration by Nb-N nanolayer and Ag nanoparticle as electron wires merely enabled a limited improvement of rate performance as reported by Kim et al..<sup>20</sup> Reshaping the morphology of Nb<sub>2</sub>O<sub>5</sub> into fine nanowire and nanosheet or integration of small Nb<sub>2</sub>O<sub>5</sub> nanoparticles into graphene matrix would seriously compromise the electrode density.<sup>14-18,21</sup> Moreover, their performance is not always better than that of well-crystallized bulk Nb<sub>2</sub>O<sub>5</sub>, since desired lattice ambience or interconnected channels may be interrupted in the defect-rich nanostructures. Bulk wiring is expected to have more homogeneous electron flux than surface wiring, however the former strategy is rarely reported. Our previous work on Nb-based oxide disclosed that solid solution phase (KNb<sub>2</sub>O<sub>5</sub>F) of KF and Nb<sub>2</sub>O<sub>5</sub> leads to a upgrade of bulk conductivity (from the darkening of powder color) and meanwhile construction of open framework tetragonal tungsten bronze (TTB) phase.<sup>22</sup> Although partial stuffing of K in open channels results in a decrease of reversible capacity, the rate and cycling performances are not bad even without intentional nanostructuring. The intercalation pseudocapacitance appears to be remarkable even for Na-storage. In fact, the conductivity improvement by introducing bronze phase is not occasional in oxyfluorides, and this effect is also confirmed in Fe-based hexagonal tungsten bronze (HTB) phase (FeF<sub>3</sub>·0.33H<sub>2</sub>O).<sup>23-25</sup>

In this work, we propose a bulk wiring strategy by introducing a small fraction of more conductive TTB related domains (KNb<sub>6</sub>O<sub>15</sub>F) to improve the rate and cycling performances of Nb<sub>2</sub>O<sub>5</sub> electrode especially the high-temperature phase (H-Nb<sub>2</sub>O<sub>5</sub>), which was thought to have the poorest rate performance among Nb<sub>2</sub>O<sub>5</sub> polymorphs

and previously abandoned as high-rate anode.<sup>13</sup> The wiring component ( $\text{KNb}_6\text{O}_{15}\text{F}$ ) has the comparable cell volume ( $1232 \text{ \AA}^3$ ) as the parent phase of  $\text{H-Nb}_2\text{O}_5$  ( $1360 \text{ \AA}^3$ ), benefiting to lattice match at phase boundary.<sup>26,27</sup> Different from conventional inactive wiring network (e.g. carbon nanotube),  $\text{KNb}_6\text{O}_{15}\text{F}$  is electroactive itself in the similar reactive voltages as  $\text{Nb}_2\text{O}_5$  and would not seriously compromise the energy density of electrode. The  $\text{KNb}_6\text{O}_{15}\text{F}$  domains are in-situ formed by doping tiny KF into  $\text{Nb}_2\text{O}_5$  lattice and uniformly embedded in micro-sized  $\text{Nb}_2\text{O}_5$ .  $\text{KNb}_6\text{O}_{15}\text{F}$ -wiring enables  $\text{H-Nb}_2\text{O}_5$  as an exceptional high-rate insertion anode without intentional nanostructuring. The reversible capacity is as high as 120, 100 and 80 mAh/g at high rates of 5C, 10C and 20C respectively in a voltage range of 1.2 and 3.0 V. The capacity can be even maintained at 50 and 35 mAh/g under extremely high 40C and 60C respectively. Compared to commercially pristine  $\text{H-Nb}_2\text{O}_5$ ,  $\text{KNb}_6\text{O}_{15}\text{F}$ -wired electrode also displays much better capacity retention and larger pseudocapacitance contribution (up to 70-90% of total stored charge).

## Experimental section

The KF doped  $\text{Nb}_2\text{O}_5$  was prepared by conventional high temperature solid state reaction method. The mixture of niobium pentaoxide (99.5%, Sinopharm) and potassium fluoride (99%, Alfa Aesar) with a molar ratio of 1:x ( $x=0.1$  or  $0.2$ ) was ground in a mortar for 1 h under air atmosphere. After grinding the mixture was coated by copper foil and put into a sealed container and was heated in a tube furnace at  $900^\circ\text{C}$  for 12 h. Then the sample was naturally cooled to room temperature to obtain the  $\text{KNb}_6\text{O}_{15}\text{F}$  wired  $\text{Nb}_2\text{O}_5$  (when  $x=0.1$ ) or  $\text{KNb}_6\text{O}_{15}\text{F}$  (when  $x=0.2$ ).

The density functional theory (DFT) calculations were performed using the plane wave basis software Vienna ab initio simulation package (VASP) within the projector-augmented wave (PAW) method. The generalized gradient approximation (GGA) of the Perdew-Burke-Ernzerhof (PBE) form was used for the exchange correlation potential. The plane-wave energy cutoff was 500 eV. The geometry optimizations were carried out with  $2 \times 2 \times 6$  Monkhorst-Pack k-grid in the first Brillouin zone. For the calculation of electronic density of states (DOS), a larger

k-grid ( $4 \times 4 \times 12$ ) was adopted with a Gaussian smearing width of 0.2 eV. In the electronic structure calculations, we set the energy convergence criteria in the order of  $10^{-4}$  eV. Structure and crystallinity of pristine, KF-doped  $\text{Nb}_2\text{O}_5$  samples and cycled electrodes of  $\text{KNb}_6\text{O}_{15}\text{F}$  wired  $\text{Nb}_2\text{O}_5$  were analyzed by X-ray diffraction (XRD, D8 Discover, Bruker) in a 2-theta range of  $5^\circ$ - $80^\circ$  at a scan rate of  $0.02^\circ/\text{s}$  using Cu  $K\alpha$  radiation. Scanning electron microscopy (SEM, Magellan 400L, FEI) measurement was performed to investigate the morphology and grain size of (un)wired powder samples, as well as corresponding element distribution by scanning transmission electron microscope (STEM) mapping technology. The morphology, structure and phase assignment of pristine and doped samples were analyzed by transmission electron microscope (TEM, JEOL JSM-6700F, operated at 200 kV) and selected area electron diffraction (SAED) technology. The component and valence state evolution of pristine, doped powders and the wired electrodes discharging to 1.2 or 0.5 V were analyzed by X-ray photoelectron spectroscopy (XPS, ESCA-lab-250) with an Al anode source. For ex situ characterization, the charged or discharged electrodes were taken out after disassembling the cycled cells in an Ar-filled glove box. These postreaction electrodes were repeatedly washed with anhydrous dimethyl carbonate (DMC) to remove the influence of the residual electrolyte. The washed electrodes were then dried in an Ar-filled glove box before further analysis.

Electrochemical experiments were performed by using CR 2032 coin cells. The working electrodes were prepared by mixing doped  $\text{Nb}_2\text{O}_5$  (or pristine  $\text{Nb}_2\text{O}_5$ ), carbon black (Super P), and poly(vinylidene fluoride) (PVDF, which is dispersed in 1-methyl-2-pyrrolidinone NMP) in a weight ratio of 7:2:1. The mixture was then ground into homogeneous slurry using mortar and pestle. The resulting slurry was pasted onto pure Cu foil (>99%) and then dried in a vacuum oven at  $80^\circ\text{C}$  for 12h. The loading mass of active material in the electrode is  $\sim 2 \text{ mg}/\text{cm}^2$ . The electrolyte consists of 1M  $\text{LiPF}_6$  dissolved in ethylene carbonate (EC) and propylene carbonate (PC) with a volume ratio of 1:1 or 1M bis(trifluoromethanesulfonimide) lithium salt ( $\text{LiTFSI}$ ) dissolved in tetraethylene glycol ether (TEGDME). Glass fibers (GF/B) from Whatman and pure lithium metal tablets were used as separators and counter

electrode, respectively. The coin cells were assembled in an argon filled glove box ( $\text{H}_2\text{O}$ ,  $\text{O}_2 < 0.1\text{ppm}$ , Vigor, Suzhou). Galvanostatic discharge-charge measurements were performed at room temperature under different rates from 0.5C to 60C (1C denotes the current density to theoretically achieve two-electron transfer within 1h for  $\text{Nb}_2\text{O}_5$ ) in a voltage range of 1.2-3.0 V or 0.5-3.0 V (vs.  $\text{Li}^+/\text{Li}$ ) on the Land multichannel battery testing system (CT2001A). Cyclic voltammetry (CV) of (un)wired electrodes was carried out at different scan rates from 0.1 to 2 mV/s in a voltage range of 1.2-3.0 V in an electrochemical workstation (VersaSTAT 3, Princeton Applied Research).

## Results and discussion

$\text{KNb}_6\text{O}_{15}\text{F}$ -wired  $\text{H-Nb}_2\text{O}_5$  was prepared by doping KF into commercially available  $\text{H-Nb}_2\text{O}_5$  in a conventional solid state reaction process at  $900^\circ\text{C}$ . Figure 1a shows the X-ray diffraction (XRD) patterns of pristine  $\text{Nb}_2\text{O}_5$ , KF-doped  $\text{Nb}_2\text{O}_5$  samples experimentally in a molar ratio of 1:10 and 1:5 for KF:  $\text{Nb}_2\text{O}_5$  respectively. Commercial  $\text{Nb}_2\text{O}_5$  is white in color and dominantly in monoclinic phase ( $\text{H-Nb}_2\text{O}_5$ , JCPDS. No. 37-1468) with minor orthorhombic phase ( $\text{T-Nb}_2\text{O}_5$ , JCPDS. No. 27-1003).<sup>27,28</sup> After KF doping, the powders become dark green and the  $\text{T-Nb}_2\text{O}_5$  phase almost disappears. Instead, in the sample by tiny KF doping (1:10 for KF:  $\text{Nb}_2\text{O}_5$ ), orthorhombic  $\text{KNb}_6\text{O}_{15}\text{F}$  (JCPDS. No. 37-0786) appears as the wiring phase and  $\text{H-Nb}_2\text{O}_5$  phase is still dominant.<sup>26</sup> Although some diffraction peaks overlap between  $\text{T-Nb}_2\text{O}_5$  and  $\text{KNb}_6\text{O}_{15}\text{F}$ , their patterns are different. The wired  $\text{H-Nb}_2\text{O}_5$  mainly consists of  $\text{KNb}_6\text{O}_{15}\text{F}$  rather than  $\text{T-Nb}_2\text{O}_5$  from the evolution of relative intensity and position of peaks after KF doping. The formation of  $\text{KNb}_6\text{O}_{15}\text{F}$  is responsible for the darkening of powder color owing to conduction upshift after KF doping. The bandgap of  $\text{KNb}_6\text{O}_{15}\text{F}$  has been estimated to be 1.64 eV by density functional theory (DFT) calculation, which is higher than that of  $\text{H-Nb}_2\text{O}_5$  (1.69 eV), also indicating a higher conductivity for the former (Figure S1). In the sample with more KF doping (1:5 for KF:  $\text{Nb}_2\text{O}_5$ ), the  $\text{KNb}_6\text{O}_{15}\text{F}$  phase becomes dominant, indicating an almost complete conversion of  $\text{H-Nb}_2\text{O}_5$  to  $\text{KNb}_6\text{O}_{15}\text{F}$ . Further increase

of KF doping amount still enables the formation of solid-solution phase of  $\text{K}(\text{Nb}_2\text{O}_5)_n\text{F}$  with decreased  $n$  value up to 1.<sup>26</sup> Our previous work has focused on  $\text{KNb}_2\text{O}_5\text{F}$  as the firstly reported energy storage electrode of TTB phase, characterized by two different stackings of pentagonal and tetragonal cavities shaped by exclusive  $\text{NbO}_5\text{F}$  octahedral chains sharing corners.<sup>22,29</sup> In this case, the structure of  $\text{KNb}_6\text{O}_{15}\text{F}$  with less K stuffing has a deviation from the ideal TTB phase. This Nb-rich phase contains Nb atoms not only in octahedral sites (5/6 Nb) but also in pentagonal bipyramids (1/6 Nb) as shown in Figure 1b.<sup>26</sup> The  $\text{NbO}_5\text{F}_2$  pentagonal bipyramids share their equatorial O-O edges with five  $\text{NbO}_6$  octahedra, which surround the regular Nb-occupied pentagonal tunnels along [001] axis.  $\text{NbO}_5\text{F}_2$  units between different a-b planes are linked by F vertices. This unique structure moiety does not compromise the stacking of sufficient pentagonal and tetragonal cavities but with evident distortion on tetragonal cavities. K atoms prefer to stay in the pentagonal cavities and the tetragonal ones remain empty.  $\text{KNb}_6\text{O}_{15}\text{F}$  has a cell volume ( $1232 \text{ \AA}^3$ ) roughly twice as large as that of  $\text{KNb}_2\text{O}_5\text{F}$  ( $629 \text{ \AA}^3$ ), mainly stemming from the remarkably increased  $a$  and  $b$  lattice parameters ( $\sim 17.6 \text{ \AA}$ ).<sup>22,26</sup> Their  $c$  lattice parameters are comparable ( $3.95\text{-}3.96 \text{ \AA}$ ).  $\text{KNb}_6\text{O}_{15}\text{F}$  has the similar structural moiety as  $\text{T-Nb}_2\text{O}_5$ , which typically consists of highly distorted  $\text{NbO}_6$  octahedra and  $\text{NbO}_7$  pentagonal bipyramids as shown in Figure 1c.<sup>13,30</sup> The distortion of  $\text{NbO}_7$  in  $\text{T-Nb}_2\text{O}_5$  appears to be more complex than  $\text{NbO}_5\text{F}_2$  in  $\text{KNb}_6\text{O}_{15}\text{F}$ , since one  $\text{NbO}_7$  shares its equatorial edges with  $\text{NbO}_6$  or another  $\text{NbO}_7$ , or with no polyhedron (i.e. leaving uncoordinated) in a-b plane.  $\text{KNb}_6\text{O}_{15}\text{F}$  displays the feature of self-supporting “room-and-pillar” framework as the case of  $\text{T-Nb}_2\text{O}_5$ . For  $\text{KNb}_6\text{O}_{15}\text{F}$ , the partial interruption of Li-ion transport pathways in a-b plane by K atoms would more or less degrade the capacity performance as confirmed later. In  $\text{H-Nb}_2\text{O}_5$ ,  $\text{NbO}_6$  octahedra sharing corners or edges are the exclusive building blocks and the characteristic pentagonal bipyramid units are absent (Figure 1d).<sup>13</sup> From the evolution of XRD patterns, it seems that the conversion to  $\text{KNb}_6\text{O}_{15}\text{F}$  with KF doping is preferential for  $\text{T-Nb}_2\text{O}_5$  than for  $\text{H-Nb}_2\text{O}_5$  in view of the structural similarity between  $\text{KNb}_6\text{O}_{15}\text{F}$  and  $\text{T-Nb}_2\text{O}_5$ . This phenomenon is also indicated by the experiment on doping KF into



pristine T-Nb<sub>2</sub>O<sub>5</sub> (Figure S2). It is found that most T-Nb<sub>2</sub>O<sub>5</sub> can be converted into KNb<sub>6</sub>O<sub>15</sub>F even under a smaller molar ratio of 1:10 for KF: Nb<sub>2</sub>O<sub>5</sub>.

X-ray photoelectron spectra (XPS) confirm the existence of K and F dopants from the emergence of K 2p and F 1s peaks (at 293 and 684.6 eV respectively) in the doped samples (Figure 2a and b). Both the K and F signals are more remarkable for KNb<sub>6</sub>O<sub>15</sub>F sample (1:5 for KF: Nb<sub>2</sub>O<sub>5</sub>) than for KNb<sub>6</sub>O<sub>15</sub>F-wired Nb<sub>2</sub>O<sub>5</sub> one (1:10 for KF: Nb<sub>2</sub>O<sub>5</sub>) due to more KF injection into the former. Nb 3d spectra of pristine H-Nb<sub>2</sub>O<sub>5</sub> have two characteristic peaks at 207.2 and 209.9 eV, assigned to Nb<sup>5+</sup> 3d<sub>5/2</sub> and Nb<sup>5+</sup> 3d<sub>3/2</sub> respectively (Figure 2c). These Nb 3d peaks are overall shifted to the positions of higher binding energy with the bonding participation of KF (e.g. Nb 3d<sub>5/2</sub> peaks around 207.3 and 207.5 eV for wired Nb<sub>2</sub>O<sub>5</sub> and KNb<sub>6</sub>O<sub>15</sub>F respectively). This phenomenon is in accordance with our previous report on KNb<sub>2</sub>O<sub>5</sub>F, which enables a more positive shift up to 208.5 eV for Nb 3d<sub>5/2</sub>.<sup>22</sup> Partial Fluorination of Nb-O into Nb-F as well as corresponding polyhedral linkage evolution should be responsible for the shift of Nb 3d signals.<sup>31</sup> Complete fluorination even results in a Nb<sup>5+</sup> 3d<sub>5/2</sub> peak with a binding energy as high as 209.4 eV as observed in K<sub>2</sub>NbF<sub>7</sub>.<sup>32</sup> Based on the element analysis by surface sensitive XPS, the ratio of K and Nb is estimated to be 10.7 and 22.8 mol% for wired Nb<sub>2</sub>O<sub>5</sub> and KNb<sub>6</sub>O<sub>15</sub>F samples respectively. The former indicates a KNb<sub>6</sub>O<sub>15</sub>F content of ~20 mol% in KNb<sub>6</sub>O<sub>15</sub>F-wired Nb<sub>2</sub>O<sub>5</sub> (at least in the surface region). The latter ratio is close to the stoichiometric ratio of K and Nb in KNb<sub>6</sub>O<sub>15</sub>F (16.7 mol%). The detected element ratio has an excess deviation from the experimentally designed ratio, indicating a slight enrichment of dopants at surface.

Figure 3a and S3 show the scanning electron microscopy (SEM) images of pristine H-Nb<sub>2</sub>O<sub>5</sub>, which consists of euhedral particles or their aggregates of several micrometers in size. These particles are characterized by distinct textured surface where aligned stripes are clearly observed, agreeing with the morphology reported by Grey et al..<sup>13</sup> From transmission electron microscopy (TEM) images (Figure 3b and S4a), it is found that the adjacent particles are welded together along their edges parallel to the stripes with greyscale contrast. Such a contrast may stem from the intergrowth of dominant H-Nb<sub>2</sub>O<sub>5</sub> and impurity T-Nb<sub>2</sub>O<sub>5</sub> with attachment of their

coherent lattice planes. Both the  $\text{Nb}_2\text{O}_5$  domains are found based on their characteristic lattice stripes assigned to (110) and (-101) planes for H- $\text{Nb}_2\text{O}_5$ , as well as to (001) and (180) planes for T- $\text{Nb}_2\text{O}_5$  from the high resolution TEM (HRTEM) images (Figure 3d and S4b). The single crystal pattern of selected area electron diffraction (SAED) corresponding to H- $\text{Nb}_2\text{O}_5$  (also pointing (110) and (-101) planes) is shown in Figure 3c.

The morphology and microstructure of  $\text{KNb}_6\text{O}_{15}\text{F}$ -wired  $\text{Nb}_2\text{O}_5$  sample show interesting evolution compared with undoped  $\text{Nb}_2\text{O}_5$ . From its SEM images in Figure 3e and S5, one can note that numerous stick-shaped particles of 50~100 nm in diameter precipitate out of original  $\text{Nb}_2\text{O}_5$ , but most of them still attach well to the parent grains in an edge-aligned way. When focusing on the delaminated stick-like grains by TEM (Figure 3f-h and S6), we observe different high-resolution lattice stripes and single crystal SAED pattern, which are assigned to (200) and (001) planes of  $\text{KNb}_6\text{O}_{15}\text{F}$  rather than any  $\text{Nb}_2\text{O}_5$  phase. It means that the newly formed stick-like grains belong to  $\text{KNb}_6\text{O}_{15}\text{F}$  phase. This result indicates a phase segregation of  $\text{KNb}_6\text{O}_{15}\text{F}$  from H- $\text{Nb}_2\text{O}_5$  in view of their potential lattice incoherence and thermal fluorination etching. Based on the similarity of structure moieties between  $\text{KNb}_6\text{O}_{15}\text{F}$  and T- $\text{Nb}_2\text{O}_5$ , T- $\text{Nb}_2\text{O}_5$  should be preferentially doped by KF and converted to  $\text{KNb}_6\text{O}_{15}\text{F}$  prior to H- $\text{Nb}_2\text{O}_5$ . This statement is also confirmed by the earlier disappearance of T- $\text{Nb}_2\text{O}_5$  XRD pattern after KF doping. The as-generated  $\text{KNb}_6\text{O}_{15}\text{F}$  can serve as a compact conductive wire in  $\text{Nb}_2\text{O}_5$  electrode network. Scanning TEM (STEM) image of  $\text{KNb}_6\text{O}_{15}\text{F}$ -wired  $\text{Nb}_2\text{O}_5$  in a dark field and the corresponding element mapping by energy dispersive X-ray spectroscopy (EDX) on the same region are shown in Figure 4a. The ratio of K and Nb is estimated to be ~5 mol% from the bulk-detectable EDX mapping, indicating that the actual fraction of  $\text{KNb}_6\text{O}_{15}\text{F}$  wires in  $\text{Nb}_2\text{O}_5$  (~10 mol%) is close to the experimentally designed ratio. The element distribution of K and F appears to be not confined in the surface sticks, indicating a bulk wiring with  $\text{KNb}_6\text{O}_{15}\text{F}$  sticks beneath. It is also possible that not all the KF-doped components are separated from H- $\text{Nb}_2\text{O}_5$ . A linear scanning across the section of two parallel sticks displays element enrichment of K and F and relatively

decreased Nb component on sticks (Figure 4b). It further suggests the synthesis of  $\text{KNb}_6\text{O}_{15}\text{F}$  preferentially on sticks.

Such an integrated wiring architecture endows  $\text{KNb}_6\text{O}_{15}\text{F}$ -decorated  $\text{Nb}_2\text{O}_5$  superior rate performance as LIB insertion anode (Figure 5). When wired  $\text{H-Nb}_2\text{O}_5$  is cycled in an electrolyte consisting of 1M  $\text{LiPF}_6$  dissolved in ethylene carbonate (EC) and propylene carbonate (PC) with a volume ratio of 1:1 in a voltage range of 1.2-3.0 V at 0.5C (Figure 5a and b), a charge capacity of 160 mAh/g is released during the first cycle with an initial coulombic efficiency (CE) of 94%. The following capacity (with a CE close to 100%) is still preserved at 140 and 120 mAh/g after 100 and 200 cycles respectively. This capacity stability is remarkably superior to that of unwired  $\text{H-Nb}_2\text{O}_5$  or pure  $\text{KNb}_6\text{O}_{15}\text{F}$  at the similar current density (in the same voltage range, Figure S7).  $\text{H-Nb}_2\text{O}_5$  has a slightly lower capacity (150 mAh/g) during the initial cycling and worse capacity retention capability with a capacity lower than 80 mAh/g after 200 cycles.  $\text{KNb}_6\text{O}_{15}\text{F}$  displays the best capacity retention with almost no degradation, however its reversible capacity is merely around 60 mAh/g due to potential K-ion blocking in diffusion channels. The capacity degradation of  $\text{H-Nb}_2\text{O}_5$  was also observed by Grey et al. even at a lower rate (0.1C).<sup>13</sup> A setting of voltage range of 1.2-3.0 V has been expected to alleviate the lattice distortion (or disruption) by limiting Li insertion number in lattices (less than the theoretical number to achieve two electron transfer). Otherwise, more Li stuffing would cause irreversible trapping of Li in distorted lattices e.g. when extending the lower cut-off voltage to 0.5 V as shown in Figure S8. Although the initial charge capacity is increased to 170 mAh/g, the following cycling undergo serious degradation with a capacity as low as 70 mAh/g after 100 cycles. Note that the voltage profiles of  $\text{KNb}_6\text{O}_{15}\text{F}$ -wired  $\text{H-Nb}_2\text{O}_5$  display a transition state between those of  $\text{H-Nb}_2\text{O}_5$  and  $\text{KNb}_6\text{O}_{15}\text{F}$ .  $\text{H-Nb}_2\text{O}_5$  is characterized by a couple of dominant well-defined plateaus around 1.7 V for both the charge and discharge processes, whereas  $\text{KNb}_6\text{O}_{15}\text{F}$  shows evidently sloped curves in the whole voltage region. Potential channel expansion or the formation of reaction sites with additionally different energy after KF doping should be responsible for the sloping of voltage curves.<sup>22</sup> For  $\text{KNb}_6\text{O}_{15}\text{F}$ -wired  $\text{H-Nb}_2\text{O}_5$ , the plateau-like feature is

still observable (around 1.7 V) in the overall sloped curves. This integrated curve feature is well preserved with the progress of cycling between 1.2 and 3.0 V. However the voltage curves become much more sloped with worse polarization and smaller capacity when discharging to lower 0.5 V. The existence of minor T-Nb<sub>2</sub>O<sub>5</sub> in commercial H-Nb<sub>2</sub>O<sub>5</sub> would not remarkably influence the electrochemical characteristic of H-Nb<sub>2</sub>O<sub>5</sub> with the preservation of staged plateaus and capacity degradation.

Similar to orthorhombic and tetragonal Nb<sub>2</sub>O<sub>5</sub>, our monoclinic phase is also robust enough to maintain its original crystal lattices with marginal change of cell volume during cycling (between 1.2 and 3.0 V),<sup>7</sup> at least from the similar XRD patterns of pristine and cycled electrodes without remarkable shift of Bragg peaks (Figure S9). The weakening of Nb<sub>2</sub>O<sub>5</sub> peaks is likely caused by lattice strain during this topotactic (solid-solution) reaction especially after lithiation. KNb<sub>6</sub>O<sub>15</sub>F appears to be more robust structurally (without remarkable weakening of corresponding XRD peaks) during electrochemical cycling. Marginal volume change enables a good integrity of wiring architecture. When discharge to 1.2 V, XPS peak of Nb 3d<sub>5/2</sub> has a negative shift of binding energy to 207.1 eV with the reduction of Nb<sup>5+</sup> (Figure S10).<sup>22</sup> The reduction is deepened with more content of Nb<sup>4+</sup> when discharge to 0.5 V as indicated from the more negative shift to 206.8 eV for Nb 3d<sub>5/2</sub>. On the other hand, the Nb 3d peaks are more intensive for the discharge state to 0.5 V than to 1.2 V, indicating a potential decomposition or attenuation of solid electrolyte interface (SEI) catalyzed by Nb<sup>4+</sup>. This may lead to the exposure of internal SEI layer with more F component from the slightly intensified F 1s peak. Excessive discharge (to 0.5 V) may cause the extrusion of K-ion by more Li stuffing from the slightly weaker K 2p peak than that to 1.2 V. More Li injection is also confirmed by stronger Li 1s peak at the lower discharge voltage.

KNb<sub>6</sub>O<sub>15</sub>F-wired H-Nb<sub>2</sub>O<sub>5</sub> displays significant superiority on rate performance compared to pristine H-Nb<sub>2</sub>O<sub>5</sub> (Figure 5c-f). Its reversible capacity (between 1.2 and 3.0 V) is as high as 120, 100 and 80 mAh/g at high rates of 5C, 10C and 20C respectively, whereas those are merely 70, 50 and 30 mAh/g at the corresponding

rates for unwired  $\text{Nb}_2\text{O}_5$ . Higher rate appears to be beneficial to alleviate the capacity decline in view of improved structure integrity and less irreversible Li-trapping at the cost of decreased capacity. (Figure S11) The former capacity can be even maintained at 50 and 35 mAh/g under extremely high 40C and 60C respectively. The polarization and symmetry of charge-discharge curves do not degrade seriously under high rates in wired electrode. For the unwired electrode, the overpotential increases dramatically when rate exceeds 1C. Even after undergoing ultrahigh-rate (20-60C) cycling, the capacity is still recoverable to ~150 mAh/g with good reversibility for wired electrode. The rate upgrade should mainly stem from the optimization of conductive network, lattice synergy as well as good rate performance of  $\text{KNb}_6\text{O}_{15}\text{F}$  wire itself as shown in Figure 5e (e.g. 30-50 mAh/g at 5-20C).

The cycling and rate performances are associated with the choice of electrolyte systems. When using the electrolyte with 1M lithium trifluoromethanesulfonate ( $\text{LiTFSI}$ ) dissolved in tetraethylene glycol dimethyl ether (TEGDME) (Figure 6), the performance gap between wired and unwired  $\text{Nb}_2\text{O}_5$  electrodes is evidently narrowed. The former displays the better capacity retention until after 100 cycles at 0.5C and merely 10-20 mAh/g higher capacity than the latter at the corresponding rates from 1C to 20C. For wired electrode, the reversible capacity is stably maintained at 120-130 mAh/g at least within 150 cycles. In contrast to carbonate electrolyte, such a cyclability improvement is not occasional in ether electrolyte and also observed in unwired sample or the system discharged to 0.5 V (Figure S12). The slightly lower capacity and worse rate performance (e.g. 90 and 40-60 mAh/g at 5C and 10-20C respectively for wired  $\text{Nb}_2\text{O}_5$ ) are likely caused by increased viscosity of ether electrolyte.  $\text{Li}^+$ -solvent co-intercalation in ether electrolyte is expected to alleviate the irreversible trapping of Li in lattices and is responsible for the better cyclability.<sup>33,34</sup> Note that the voltage profiles of corresponding electrodes are similar for both the electrolyte systems (Figure S13).

The observed capacity decline of  $\text{H-Nb}_2\text{O}_5$  is not abnormal and also observed in other reports (e.g. by Grey et al.).<sup>13</sup>  $\text{KNb}_6\text{O}_{15}\text{F}$ -wiring has remarkably improved the capacity retention compared with the counterpart without this wiring, however the

gradual capacity decline still exists. The capacity decline is associated with the crystalline structure, choice of electrolyte and setting of cut-off voltage. The high-temperature phase (H-Nb<sub>2</sub>O<sub>5</sub>) has potential strain evolution during cycling as indicated from the staged plateaus, which would more or less cause irreversible Li-ion trapping or grain cracking. In contrast, metastable bronze phase (T-Nb<sub>2</sub>O<sub>5</sub>) and KNb<sub>6</sub>O<sub>15</sub>F show sloped curves, indicating less strain evolution, which is responsible for the better capacity retention. Therefore the wiring by KNb<sub>6</sub>O<sub>15</sub>F enables a slow-down of capacity decline for H-Nb<sub>2</sub>O<sub>5</sub>. Since the capacity degradation for KNb<sub>6</sub>O<sub>15</sub>F is negligible (Figure 5b), increasing the KF doping amount is expected to enable a further improvement on cycling stability. However this would compromise the absolute capacity with the increase of KNb<sub>6</sub>O<sub>15</sub>F ratio in composite, as the capacity of pure KNb<sub>6</sub>O<sub>15</sub>F is not high (~60 mAh/g). The employ of LiTFSI-TEGDME also enables a better cycling stability in view of its potential effect on suppressing irreversible Li-trapping as a consequence of Li<sup>+</sup>-solvent co-intercalation in ether electrolyte. The injection of more Li-ions by decreasing the lower cut-off voltage would undoubtedly increase the structure instability as shown in the case of discharging to 0.5 V (Figure S8). Therefore we uplift the lower cut-off voltage to 1.2 V in order to maintain the structure integrity however at the cost of specific capacity shrinkage. The capacity performance of KNb<sub>6</sub>O<sub>15</sub>F-wired H-Nb<sub>2</sub>O<sub>5</sub> is not bad compared with the reported T-Nb<sub>2</sub>O<sub>5</sub> if based on the same cut-off voltage of 1.2 V.<sup>13</sup>

This unexceptional rate performance of wired H-Nb<sub>2</sub>O<sub>5</sub> appears to be related to pseudocapacitive effect. Cyclic voltammetry (CV) curves at various scan rates from 0.1 to 2 mV/s are obtained to quantitatively check the pseudocapacitance contribution during (de)intercalation process (Figure 7).<sup>4,9-11</sup> The CV curves are in good accordance with the galvanostatic charge-discharge ones. Pristine H-Nb<sub>2</sub>O<sub>5</sub> displays roughly two couples of redox peaks around 1.7 and 2.0 V respectively. The former peaks are much more intensive but with larger voltage polarization between anodic and cathodic processes compared with the latter ones. After KNb<sub>6</sub>O<sub>15</sub>F wiring, the CV profile becomes smooth with mainly a couple of broader redox peaks still around 1.7

V instead of staged sharp peaks. The broadening of CV peaks is contributed by the  $\text{KNb}_6\text{O}_{15}\text{F}$  phase component typical of broad peaks, which overlap with the relatively sharp CV peaks of  $\text{H-Nb}_2\text{O}_5$  and therefore smoothen the overall peak profiles for  $\text{KNb}_6\text{O}_{15}\text{F}$ -wired  $\text{H-Nb}_2\text{O}_5$ . Such an evolution of electrochemical curves is also observed from the charge-discharge measurement. The staged plateaus in  $\text{H-Nb}_2\text{O}_5$  become less evident after wiring of  $\text{KNb}_6\text{O}_{15}\text{F}$ , since the latter imposes the sloped curves in the similar voltage range as that of  $\text{H-Nb}_2\text{O}_5$ . The type of electrochemical process can be deduced from  $i(V) = av^b$  (or  $\log i(V) = b \log v + \log a$ ), where current ( $i$ ) as a function of potential ( $V$ ) obeys a power law relationship with scan rate ( $v$ ) with  $a$  and  $b$  as adjustable parameters. In view of overpotential change with scan rate, the independent variable potential is slightly adjusted based on equidistribution principle. The  $b$ -value is determined from the slope of the plots of  $\log i$  vs.  $\log v$  (e.g. insets of Figure 7a and b for corresponding peak positions). It approaches 1.0 if the process is capacitance-dominated, whereas closing to 0.5 if diffusion-controlled (i.e. faradaic intercalation).<sup>35,36</sup> As seen, the  $b$ -values ( $\sim 0.7$ ) lie in the middle between 0.5 and 1 from the near-linear fitting of  $\log i$ - $\log v$  plots in the whole rate range, indicating an involvement of remarkable capacitance contribution. Further,  $i(V) = k_1v + k_2v^{1/2}$  (or  $i(V)/v^{1/2} = k_1v^{1/2} + k_2$ ) is used to calculate the respective current contributions from capacitive effect ( $k_1v$ ) and intercalation process ( $k_2v^{1/2}$ ). Both the parameters  $k_1$  and  $k_2$  are determined from the linear relationship of  $iv^{-1/2}$  and  $v^{1/2}$ . The typical CV curves at 1 mV/s are shown in Figure 7c and d with the outlined capacitive current ( $k_1v$ , integrated into orange area) distinguished from the total current ( $k_1v + k_2v^{1/2}$ ). The ratio of stored charge contributed by capacitive current at respective scan rates is shown in Figure 7e and f. The fraction of capacitive contribution is high for wired  $\text{H-Nb}_2\text{O}_5$ , increasing from 72.6 % at 0.1 mV/s to 94.2 % at 2 mV/s, whereas it is lower for unwired one (from 65 % at 0.1 mV/s to 84 % at 2 mV/s). A higher fraction of capacitive contribution in the former is responsible for its better rate performance.

Since no intentional nanostructuring has been applied, a high fraction of capacitive contribution can be ascribed to the intrinsic intercalation pseudocapacitance in open channels especially of wired phase  $\text{KNb}_6\text{O}_{15}\text{F}$  and

impurity T-Nb<sub>2</sub>O<sub>5</sub>.<sup>9-11,22,37-39</sup> Both the wiring components are of the “room-and-pillar” framework with the coexistence of NbO<sub>6</sub> octahedra and NbO<sub>5</sub>F<sub>2</sub> (or NbO<sub>7</sub>) pentagonal bipyramids.<sup>13,22</sup> The TTB related structure endows KNb<sub>6</sub>O<sub>15</sub>F potential open channels of more dimensionality not only along the a-b plane and but also the [001] direction. This structure in dark green color appears to be more conductive than T-Nb<sub>2</sub>O<sub>5</sub> in white color. Therefore KNb<sub>6</sub>O<sub>15</sub>F is expected to enable a higher pseudocapacitance fraction and the tolerance of extremely high rates, although its absolute capacity is not high due to partial blocking of channels by K atoms. In the wired sample, a small content of KNb<sub>6</sub>O<sub>15</sub>F (~10 mol%) would not compromise the capacity performance and on the contrary it is sufficient to guarantee an extraordinary rate performance. It is a big challenge to effectively wire micro-sized particles of irregular shape. The in-situ precipitation of KNb<sub>6</sub>O<sub>15</sub>F stick-like wires with most lying laterally fortunately maximizes the contact with parent grains and electron fluxing. Some detached KNb<sub>6</sub>O<sub>15</sub>F sticks can also serve as electron transport bridges between Nb<sub>2</sub>O<sub>5</sub> particles, enabling the further strengthening of conductive network. Marginal lithiation is enough to activate the conductivity of bulk Nb<sub>2</sub>O<sub>5</sub> particles, which are no longer the bottleneck of intragrain charge transport.<sup>10</sup> Such a strategy of in-situ precipitation and construction of conductive wires can be extended to other (micro-sized) electrode systems.

## Conclusion

In summary, we reported an exceptional high-rate intercalation anode consisting of high-temperature phase H-Nb<sub>2</sub>O<sub>5</sub> wired by tetragonal tungsten bronze (TTB) related KNb<sub>6</sub>O<sub>15</sub>F domains. Different from conventional inactive wiring network based on nanocarbon, robust KNb<sub>6</sub>O<sub>15</sub>F as stick-like wire is electroactive itself and moreover of high rate in the similar voltage zone as Nb<sub>2</sub>O<sub>5</sub>. Therefore it would not compromise the energy density and on the contrary is beneficial to the power density and cyclability of electrode. These conductive TTB related domains are in-situ formed and precipitated by doping a small fraction of KF into H-Nb<sub>2</sub>O<sub>5</sub> lattice. Their optimized distribution is



caused by original constraint of lattice alignment and enables the enhancement of electron fluxing not only between grains but also inside of grains. The wired electrode can achieve a reversible capacity as high as 120, 100 and 80 mAh/g at 5C, 10C and 20C respectively between 1.2 and 3.0 V. The capacity of 35-50 mAh/g is obtainable even under extremely high 40-60C. Large fraction of intercalation pseudocapacitance (up to 70-90% of total stored charge) contributes to the superior rate performance.

## ASSOCIATED CONTENT

### Supporting Information

DFT calculation of bandgap of  $\text{KNb}_6\text{O}_{15}\text{F}$  and  $\text{H-Nb}_2\text{O}_5$ , XRD of pristine and KF-doped  $\text{T-Nb}_2\text{O}_5$ , SEM and TEM of pristine  $\text{H-Nb}_2\text{O}_5$ , SEM and TEM of  $\text{KNb}_6\text{O}_{15}\text{F}$ -wired  $\text{H-Nb}_2\text{O}_5$ , charge-discharge curves of pristine  $\text{H-Nb}_2\text{O}_5$  and  $\text{KNb}_6\text{O}_{15}\text{F}$ , cycling performance and charge-discharge curves of  $\text{KNb}_6\text{O}_{15}\text{F}$ -wired  $\text{H-Nb}_2\text{O}_5$ , XRD of pristine and cycled  $\text{KNb}_6\text{O}_{15}\text{F}$ -wired  $\text{H-Nb}_2\text{O}_5$  electrodes, XPS of cycled  $\text{KNb}_6\text{O}_{15}\text{F}$ -wired  $\text{H-Nb}_2\text{O}_5$  electrodes, cycling performance and charge-discharge curves of  $\text{KNb}_6\text{O}_{15}\text{F}$ -wired  $\text{H-Nb}_2\text{O}_5$  in LiTFSI-TEGDME, charge-discharge curves of pristine  $\text{H-Nb}_2\text{O}_5$  and  $\text{KNb}_6\text{O}_{15}\text{F}$  in LiTFSI-TEGDME. This material is available free of charge via the Internet at <http://pubs.acs.org>.

## AUTHOR INFORMATION

### Notes

The authors declare no competing financial interest.

## ACKNOWLEDGEMENTS

This work was supported by National Key Research and Development Program under Grant No. 2016YFB0901600, National Natural Science Foundation of China under Grant No. 51372263, Key Research Program of Chinese Academy of Sciences under Grant No. KGZD-EW-T06 and “Hundred Talents” Program of Chinese Academy of

Sciences. The authors thank H. H. Chen and J. Tian for helpful discussion.

## References

- (1) Li, C. L.; Gu, L.; Tong, J. W.; Maier, J. Carbon Nanotube Wiring of Electrodes for High-Rate Lithium Batteries Using an Imidazolium-Based Ionic Liquid Precursor as Dispersant and Binder: A Case Study on Iron Fluoride Nanoparticles. *ACS Nano* **2011**, *5*, 2930-2938.
- (2) Mai, L. Q.; Tian, X. C.; Xu, X.; Chang, L.; Xu, L. Nanowire Electrodes for Electrochemical Energy Storage Devices. *Chem. Rev.* **2014**, *114*, 11828-11862.
- (3) Wei, Q. L.; Xiong, F. Y.; Tan, S. S.; Huang, L.; Lan, E. H.; Dunn, B.; Mai, L. Q. Porous One-Dimensional Nanomaterials: Design, Fabrication and Applications in Electrochemical Energy Storage. *Adv. Mater.* **2017**, 201602300.
- (4) Yu, P. F.; Li, C. L.; Guo, X. X. Sodium Storage and Pseudocapacitive Charge in Textured  $\text{Li}_4\text{Ti}_5\text{O}_{12}$  Thin Films. *J. Phys. Chem. C* **2014**, *118*, 10616-10624.
- (5) Naoi, K.; Kurita, T.; Abe, M.; Furuhashi, T.; Abe, Y.; Okazaki, K.; Miyamoto, J.; Iwama, E.; Aoyagi, S.; Naoi, W.; Simon, P. Ultrafast Nanocrystalline- $\text{TiO}_2(\text{B})$ /Carbon Nanotube Hyperdispersion Prepared via Combined Ultracentrifugation and Hydrothermal Treatments for Hybrid Supercapacitors. *Adv. Mater.* **2016**, *28*, 6751-6757.
- (6) Odziomek, M.; Chaput, F.; Rutkowska, A.; Swierczek, K.; Olszewska, D.; Sitarz, M.; Lerouge, F.; Parola, S. Hierarchically Structured Lithium Titanate for Ultrafast Charging in Long-Life High Capacity Batteries. *Nat. Commun.* **2017**, *8*, 15636.
- (7) Kodama, R.; Terada, Y.; Nakai, I.; Komaba, S.; Kumagai, N. Electrochemical and In Situ XAFS-XRD Investigation of  $\text{Nb}_2\text{O}_5$  for Rechargeable Lithium Batteries. *J. Electrochem. Soc.* **2006**, *153*, A583-A588.
- (8) Usui, H.; Yoshioka, S.; Wasada, K.; Shimizu, M.; Sakaguchi, H. Nb-Doped Rutile

- TiO<sub>2</sub>: A Potential Anode Material for Na-Ion Battery. *ACS Appl. Mater. Interfaces* **2015**, *7*, 6567-6573.
- (9) Augustyn, V.; Come, J.; Lowe, M. A.; Kim, J. W.; Taberna, P. L.; Tolbert, S. H.; Abruna, H. D.; Simon, P.; Dunn, B. High-Rate Electrochemical Energy Storage through Li<sup>+</sup> Intercalation Pseudocapacitance. *Nat. Mater.* **2013**, *12*, 518-522.
- (10) Kim, J. W.; Augustyn, V.; Dunn, B. The Effect of Crystallinity on the Rapid Pseudocapacitive Response of Nb<sub>2</sub>O<sub>5</sub>. *Adv. Energy Mater.* **2012**, *2*, 141-148.
- (11) Come, J.; Augustyn, V.; Kim, J. W.; Rozier, P.; Taberna, P. L.; Gogotsi, P.; Long, J. W.; Dunn, B.; Simon, P. Electrochemical Kinetics of Nanostructured Nb<sub>2</sub>O<sub>5</sub> Electrodes. *J. Electrochem. Soc.* **2014**, *161*, A718-A725.
- (12) Lubimtsev, A. A.; Kent, P. R. C.; Sumpter, B. G.; Ganesh, P. Understanding the Origin of High-Rate Intercalation Pseudocapacitance in Nb<sub>2</sub>O<sub>5</sub> Crystals. *J. Mater. Chem. A* **2013**, *1*, 14951-14956.
- (13) Griffith, K. J.; Forse, A. C.; Griffin, J. M.; Grey, C. P. High-Rate Intercalation without Nanostructuring in Metastable Nb<sub>2</sub>O<sub>5</sub> Bronze Phases. *J. Am. Chem. Soc.* **2016**, *138*, 8888-8899.
- (14) Kong, L. P.; Zhang, C. F.; Wang, J. T.; Qiao, W. M.; Ling, L. C.; Long, D. H. Free-Standing T-Nb<sub>2</sub>O<sub>5</sub>/Graphene Composite Papers with Ultrahigh Gravimetric/Volumetric Capacitance for Li-Ion Intercalation Pseudocapacitor. *ACS Nano* **2015**, *9*, 11200-11208.
- (15) Zhang, H. M.; Wang, Y.; Liu, P.; Chou, S. L.; Wang, J. Z.; Liu, H. W.; Wang, G. Z.; Zhao, H. J. Highly Ordered Single Crystalline Nanowire Array Assembled Three-Dimensional Nb<sub>3</sub>O<sub>7</sub>(OH) and Nb<sub>2</sub>O<sub>5</sub> Superstructures for Energy Storage and Conversion Applications. *ACS Nano* **2016**, *10*, 507-514.
- (16) Rahman, M. M.; Rani, R. A.; Sadek, A. Z.; Zoolfakar, A. S.; Field, M. R.; Ramireddy, T.; Kalantar-zadeh, K.; Chen, Y. A Vein-Like Nanoporous Network of Nb<sub>2</sub>O<sub>5</sub> with A Higher Lithium Intercalation Discharge Cut-Off Voltage. *J. Mater. Chem. A* **2013**, *1*, 11019-11025.
- (17) Song, M. Y.; Kim, N. R.; Yoon, H. J.; Cho, S. Y.; Jin, H. J.; Yun, Y. S. Long-Lasting Nb<sub>2</sub>O<sub>5</sub>-Based Nanocomposite Materials for Li-Ion Storage. *ACS*

*Appl. Mater. Interfaces* **2017**, 9, 2267-2274.

- (18) Liu, M. N.; Yan, C.; Zhang, Y. G. Fabrication of Nb<sub>2</sub>O<sub>5</sub> Nanosheets for High-rate Lithium Ion Storage Applications. *Sci. Rep.* **2015**, 5, 8326.
- (19) Cava, R. J.; Batlogg, B.; Krajewski, J. J.; Poulsen, H. F.; Gammel, P.; Peck, W. F.; Rupp, L. W. Electrical and Magnetic Properties of Nb<sub>2</sub>O<sub>5-δ</sub> Crystallographic Shear Structures. *Phys. Rev. B* **1991**, 44, 6973.
- (20) Cheong, J. Y.; Kim, C.; Jung, J. W.; Yoon, K. R.; Cho, S. H.; Youn, D. Y.; Jang, H. Y.; Kim, I. D. Formation of a Surficial Bifunctional Nanolayer on Nb<sub>2</sub>O<sub>5</sub> for Ultrastable Electrodes for Lithium-Ion Battery. *Small* **2017**, 13, 1603610.
- (21) Li, H. S.; Zhu, Y.; Dong, S. Y.; Shen, L. F.; Chen, Z. J.; Zhang, X. G.; Yu, G. H. Self-Assembled Nb<sub>2</sub>O<sub>5</sub> Nanosheets for High Energy-High Power Sodium Ion Capacitors. *Chem. Mater.* **2016**, 28, 5753-5760.
- (22) Han, Y. L.; Yang, M. H.; Zhang, Y.; Xie, J. J.; Yin, D. G.; Li, C. L. Tetragonal Tungsten Bronze Framework as Potential Anode for Na-Ion Batteries. *Chem. Mater.* **2016**, 28, 3139-3147.
- (23) Li, C. L.; Gu, L.; Tsukimoto, S.; van Aken, P. A.; Maier, J. Low-Temperature Ionic-Liquid-Based Synthesis of Nanostructured Iron-Based Fluoride Cathodes for Lithium Batteries. *Adv. Mater.* **2010**, 22, 3650-3654.
- (24) Li, C. L.; Gu, L.; Tong, J. W.; Tsukimoto, S.; Maier, J. A Mesoporous Iron-Based Fluoride Cathode of Tunnel Structure for Rechargeable Lithium Batteries. *Adv. Funct. Mater.* **2011**, 21, 1391-1397.
- (25) Li, C. L.; Yin, C. L.; Mu, X. K.; Maier, J. Top-Down Synthesis of Open Framework Fluoride for Lithium and Sodium Batteries. *Chem. Mater.* **2013**, 25, 962-969.
- (26) Li, D. Y.; Lundberg, M.; Werner, P. E.; Westdahl, M. Occurrence of The Tetragonal Tungsten Bronze Structure Type in The KF-Nb<sub>2</sub>O<sub>5</sub> System. *Acta Chem. Scand. A* **1984**, 38, 813-817.
- (27) Kato, K. Structure Refinement of H-Nb<sub>2</sub>O<sub>5</sub>. *Acta Cryst.* **1976**, B32, 764-767.
- (28) Kato, K.; Tamura, S. Die Kristallstruktur von T-Nb<sub>2</sub>O<sub>5</sub>. *Acta Cryst.* **1975**, B31, 673-677.

- (29) Magneli, A.; Nord, S. Bronze-Type Structure of  $\text{KNb}_2\text{O}_5\text{F}$  and  $\text{KTa}_2\text{O}_5\text{F}$ . *Acta Chem. Scand.* **1976**, *19*, 1510-1510.
- (30) Chen, D. C.; Wang, J. H.; Chou, T. F.; Zhao, B.; El-Sayed, M. A.; Liu, M. L. Unraveling the Nature of Anomalously Fast Energy Storage in  $\text{T-Nb}_2\text{O}_5$ . *J. Am. Chem. Soc.* **2017**, *139*, 7071-7081.
- (31) Fontaine, R.; Caillat, R.; Feve, L.; Guittet, M. J. Déplacement chimique ESCA dans la série des oxydes du niobium. *J. Electron Spectrosc.* **1977**, *10*, 349-357.
- (32) McGuire, G. E.; Schweitzer, G. K.; Carlson, T. A. Core Electron Binding Energies in some Group IIIA, VB, and VIB Compound. *Inorg. Chem.* **1973**, *12*, 2450-2453.
- (33) Kim, H.; Hong, J.; Park, Y. U.; Kim, J.; Hwang, I.; Kang, K. Sodium Storage Behavior in Natural Graphite using Ether-Based Electrolyte Systems. *Adv. Funct. Mater.* **2015**, *25*, 534-541.
- (34) Moon, H.; Tatara, R.; Mandai, T.; Ueno, K.; Yoshida, K.; Tachikawa, N.; Yasuda, T.; Dokko, K.; Watanabe, M. Mechanism of Li Ion Desolvation at the Interface of Graphite Electrode and Glyme-Li Salt Solvate Ionic Liquids. *J. Phys. Chem. C* **2014**, *118*, 20246-20256.
- (35) Lindstrom, H.; Sodergren, S.; Solbrand, A.; Rensmo, H.; Hjelm, J.; Hagfeldt, A.; Lindquist, S. E.  $\text{Li}^+$  Ion Insertion in  $\text{TiO}_2$  (Anatase). 2. Voltammetry on Nanoporous Films. *J. Phys. Chem. B* **1997**, *101*, 7717-7722.
- (36) Bard, A. J.; Faulkner, L. R. *Electrochemical Method: Fundamentals and Applications*, John Wiley & Sons: New York, **1980**.
- (37) Sun, H. T.; Mei, L.; Liang, J. F.; Zhao, Z. P.; Lee, C.; Fei, H. L.; Ding, M. N.; Lau, J.; Li, M. F.; Wang, C.; Xu, X.; Hao, G. L.; Papandrea, B.; Shakir, I.; Dunn, B.; Huang, Y.; Duan, X. F. Three-Dimensional Holey-Graphene Niobia Composite Architectures for Ultrahigh-Rate Energy Storage. *Science* **2017**, *356*, 599-604.
- (38) Song, H.; Fu, J. J.; Ding, K.; Huang, C.; Wu, K.; Zhang, X. M.; Gao, B.; Huo, K. F.; Peng, X.; Chu, P. K. Flexible  $\text{Nb}_2\text{O}_5$  Nanowires/Graphene Film Electrode for High Performance Hybrid Li-Ion Supercapacitors. *J. Power Sources* **2016**, *328*, 599-606.

(39) Lübke, M.; Sumboja, A.; Johnson, I. D.; Brett, D. J. L.; Shearing, P. R.; Liu, Z. L.; Darr, J. A. High Power Nano-Nb<sub>2</sub>O<sub>5</sub> Negative Electrodes for Lithium-Ion Batteries. *Electrochim. Acta* **2016**, *192*, 363-369.

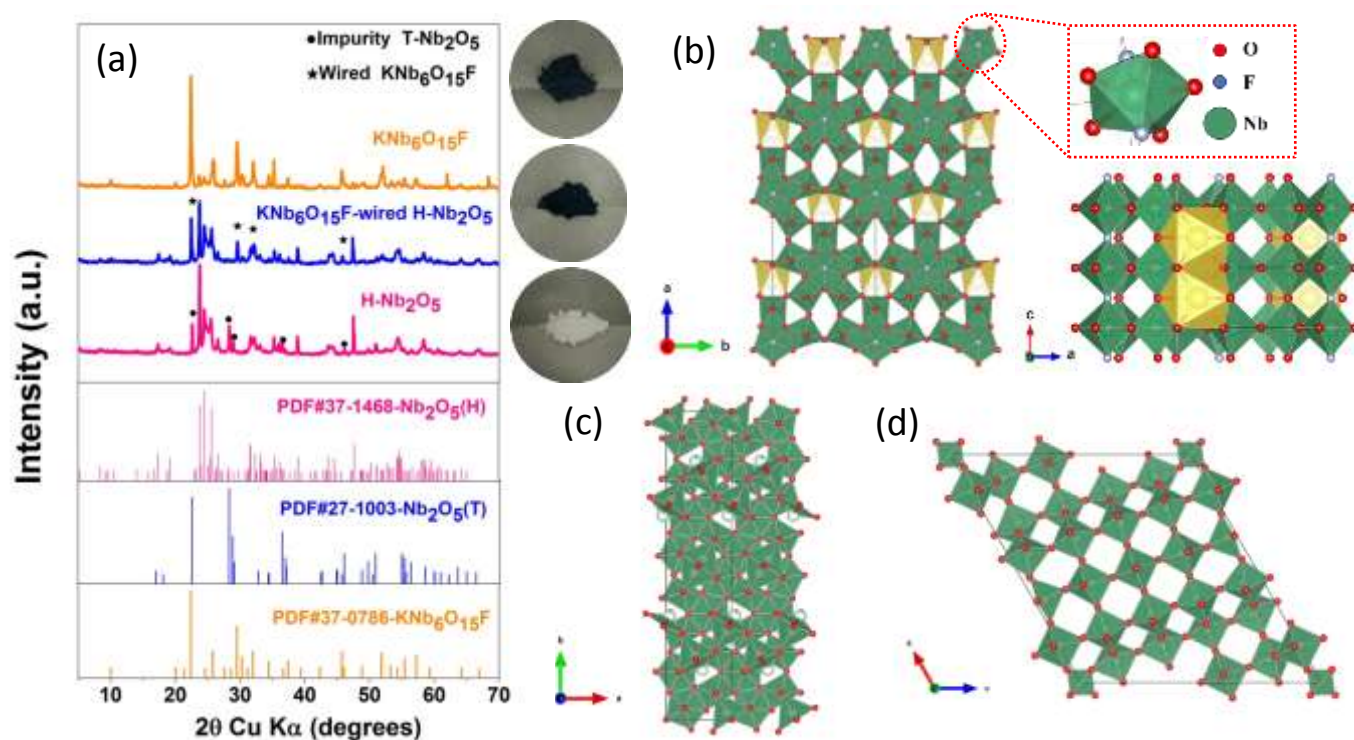


**Figure 1.** (a) XRD patterns of pristine Nb<sub>2</sub>O<sub>5</sub>, KNb<sub>6</sub>O<sub>15</sub>F-wired H-Nb<sub>2</sub>O<sub>5</sub> and KNb<sub>6</sub>O<sub>15</sub>F samples. The standard patterns of H-Nb<sub>2</sub>O<sub>5</sub>, T-Nb<sub>2</sub>O<sub>5</sub> and KNb<sub>6</sub>O<sub>15</sub>F are also listed as references. The latter two KF-doped samples are experimentally in a molar ratio of 1:10 and 1:5 for KF: Nb<sub>2</sub>O<sub>5</sub> respectively. The powders become dark green from white in color after KF doping. Crystallographic structures of (b) KNb<sub>6</sub>O<sub>15</sub>F, (c) T-Nb<sub>2</sub>O<sub>5</sub> and (d) H-Nb<sub>2</sub>O<sub>5</sub> with Nb-O and Nb-O-F polyhedrons in green, O atoms in red, F atoms in blue and K atoms in yellow. KNb<sub>6</sub>O<sub>15</sub>F and T-Nb<sub>2</sub>O<sub>5</sub> consist of similar structural moieties with coexistence of NbO<sub>6</sub> octahedra and NbO<sub>7</sub> (NbO<sub>5</sub>F<sub>2</sub>) pentagonal bipyramids, which are absent in H-Nb<sub>2</sub>O<sub>5</sub>.

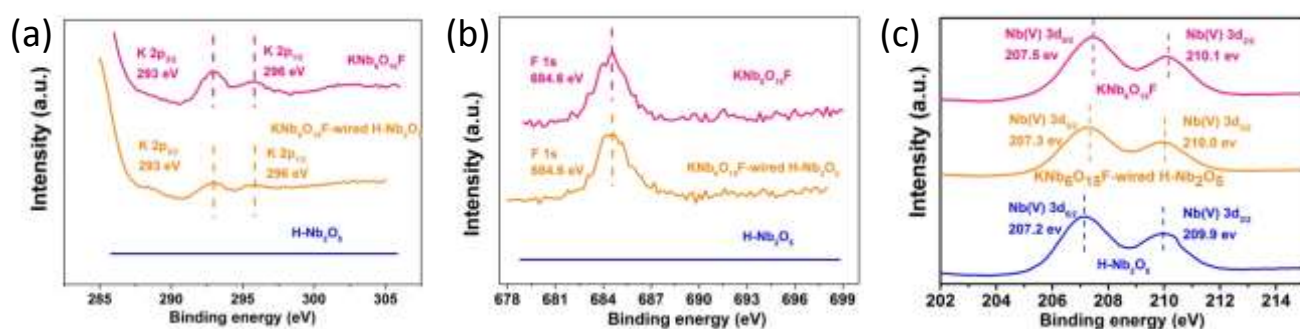


**Figure 2.** XPS of (a) K 2p, (b) F 1s and (c) Nb 3d in unwired and wired  $\text{Nb}_2\text{O}_5$  samples with different KF doping amounts.

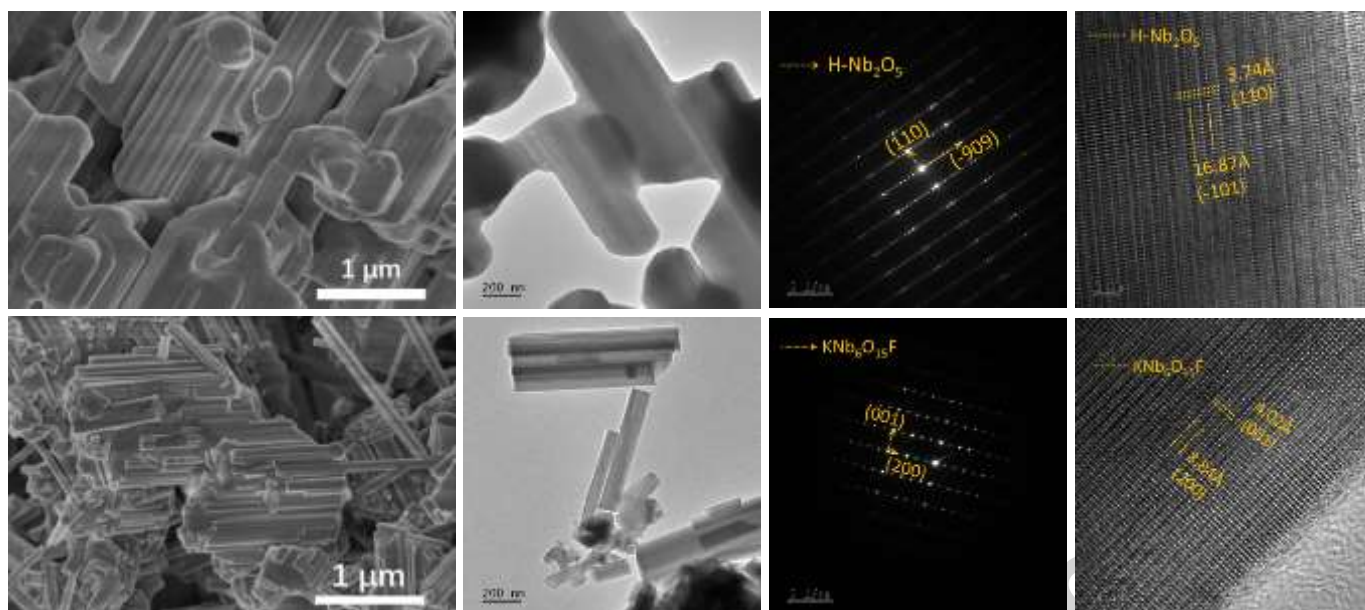


**Figure 3.** (a) SEM image, (b) TEM image, (c) SAED pattern and (d) HRTEM image of pristine  $\text{Nb}_2\text{O}_5$ , which consists of welded euhedral particles of several micrometers in size. (e) SEM image, (f) TEM image, (g) SAED pattern and (h) HRTEM image of  $\text{KNb}_6\text{O}_{15}\text{F}$ -wired  $\text{Nb}_2\text{O}_5$ , which consists of numerous stick-shaped particles of 50~100 nm in diameter with most of them attached to parent grains in an edge-aligned way. The newly formed stick-like grains belong to  $\text{KNb}_6\text{O}_{15}\text{F}$  wiring phase.



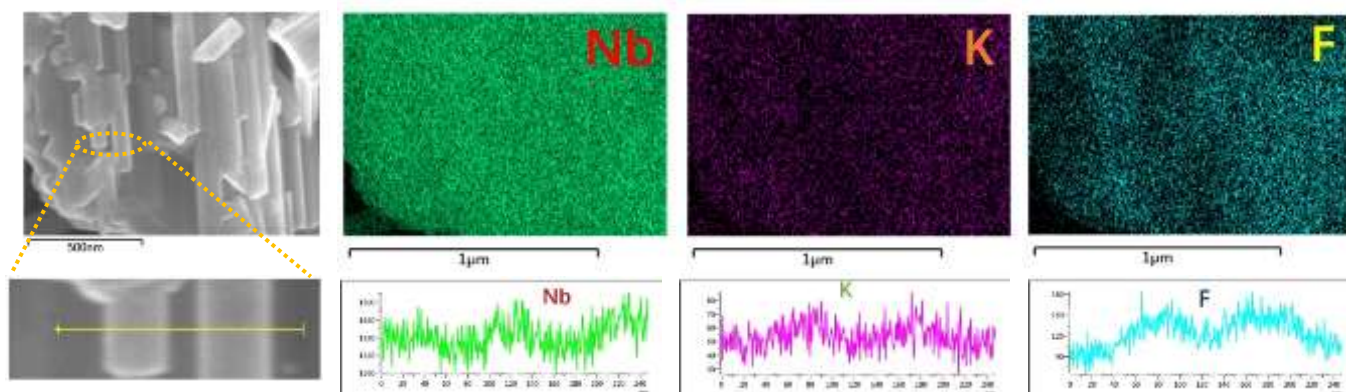


**Figure 4.** (a) STEM image of KNb<sub>6</sub>O<sub>15</sub>F-wired Nb<sub>2</sub>O<sub>5</sub> and element mapping of Nb, K and F by EDX. (b) Element linear scanning of corresponding region in KNb<sub>6</sub>O<sub>15</sub>F-wired Nb<sub>2</sub>O<sub>5</sub>.

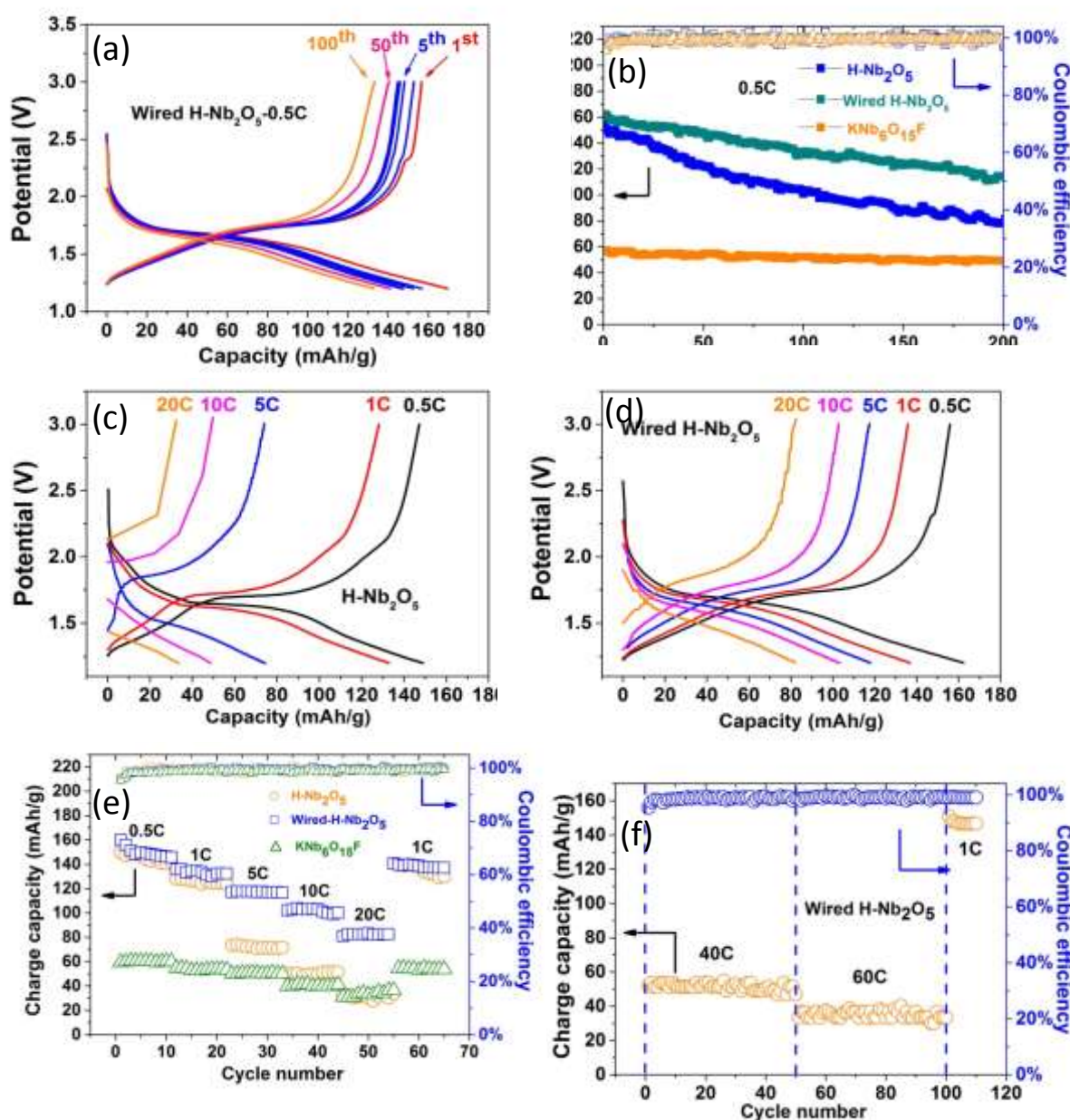


**Figure 5.** (a) Galvanostatic charge-discharge curves of  $\text{KNb}_6\text{O}_{15}\text{F}$ -wired  $\text{H-Nb}_2\text{O}_5$  at 0.5 C in a voltage range of 1.2-3.0 V during the first five cycles, 50<sup>th</sup> and 100<sup>th</sup> cycles. The electrolyte is  $\text{LiPF}_6\text{-EC-PC}$ . (b) Charge capacity and coulombic efficiency as a function of cycle number for pristine  $\text{Nb}_2\text{O}_5$ ,  $\text{KNb}_6\text{O}_{15}\text{F}$ -wired  $\text{H-Nb}_2\text{O}_5$  and  $\text{KNb}_6\text{O}_{15}\text{F}$  electrodes at 0.5 C. The wired  $\text{Nb}_2\text{O}_5$  displays the best capacity retention. Charge-discharge curves of (c) unwired and (d) wired  $\text{Nb}_2\text{O}_5$  electrodes depending on different rates from 0.5C to 20C. (e) Rate performance comparison among pristine  $\text{Nb}_2\text{O}_5$ ,  $\text{KNb}_6\text{O}_{15}\text{F}$ -wired  $\text{H-Nb}_2\text{O}_5$  and  $\text{KNb}_6\text{O}_{15}\text{F}$  electrodes. (f) Rate performance of wired  $\text{Nb}_2\text{O}_5$  at ultrahigh rates of 40 C and 60 C.

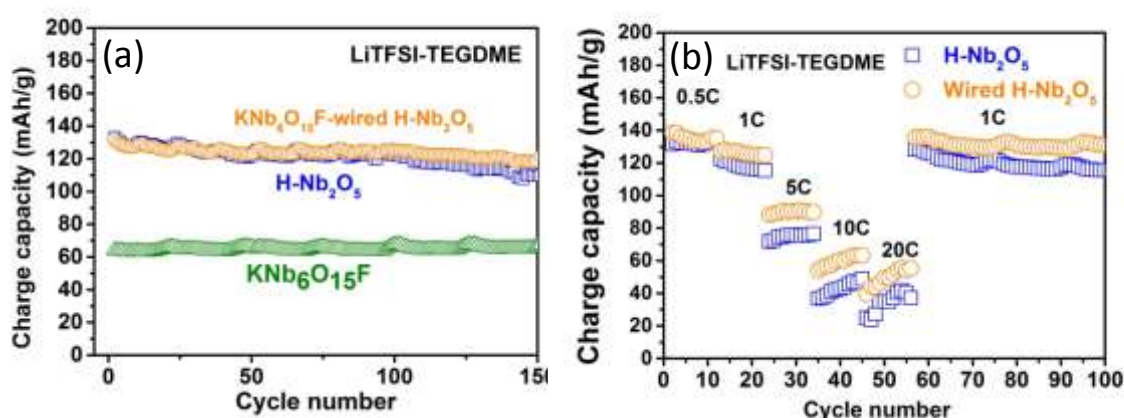


**Figure 6.** (a) Charge capacity as a function of cycle number for pristine  $\text{Nb}_2\text{O}_5$ ,  $\text{KNb}_6\text{O}_{15}\text{F}$ -wired  $\text{H-Nb}_2\text{O}_5$  and  $\text{KNb}_6\text{O}_{15}\text{F}$  electrodes at 0.5 C in a reference electrolyte of LiTFSI-TEGDME. (b) Rate performance comparison between unwired and wired  $\text{Nb}_2\text{O}_5$  from 0.5 C to 20 C in LiTFSI-TEGDME.

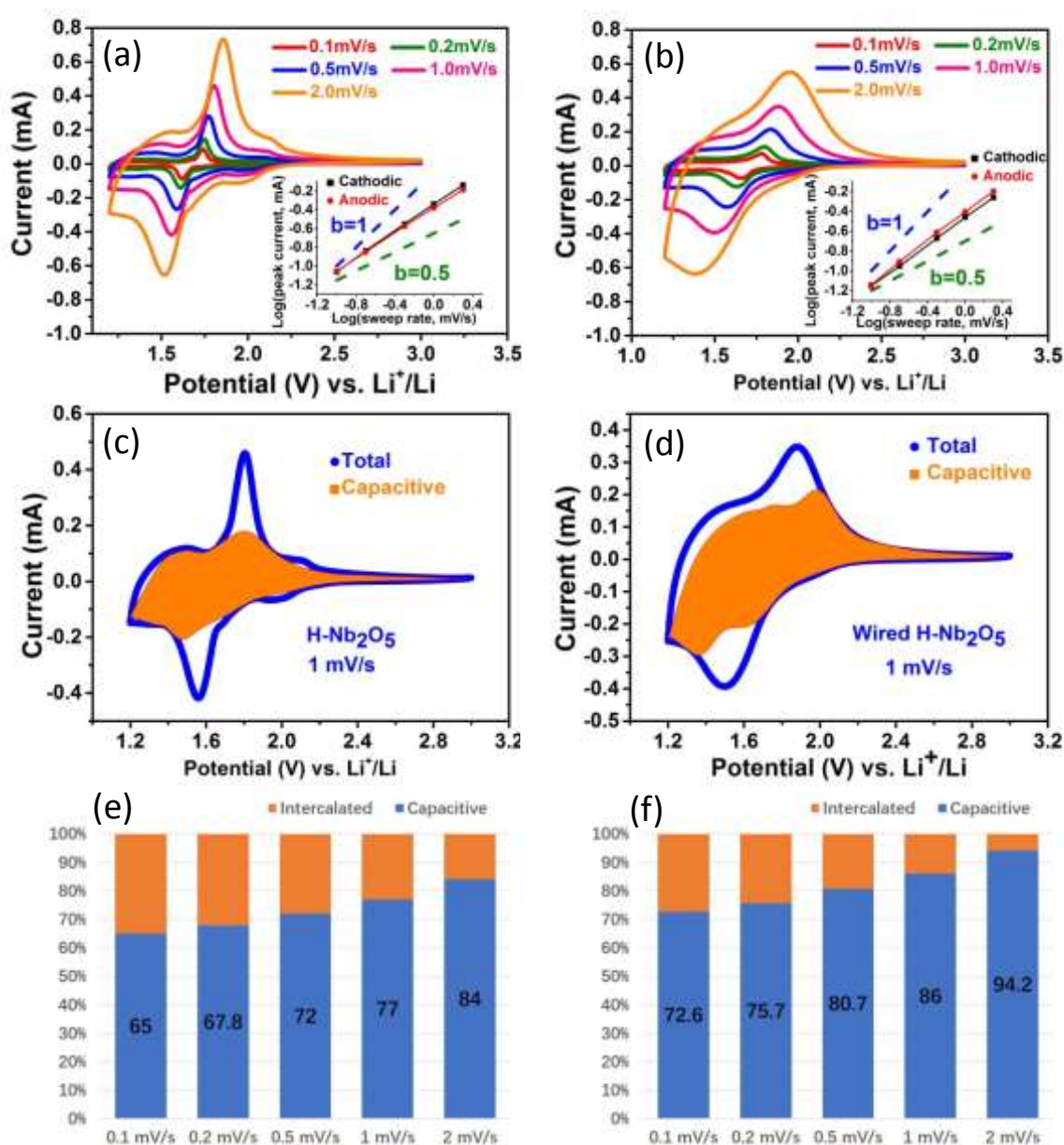


**Figure 7.** CV curves of (a) pristine  $\text{Nb}_2\text{O}_5$  and (b)  $\text{KNb}_6\text{O}_{15}\text{F}$ -wired  $\text{H-Nb}_2\text{O}_5$  at various scan rates from 0.1 to 2.0 mV/s between 1.2 and 3.0 V. Insets: power law dependence of measured current on scan rate at corresponding peak potentials based on  $\log i(V) = b \log v + \log a$ . CV curves of (c) pristine  $\text{Nb}_2\text{O}_5$  and (d)  $\text{KNb}_6\text{O}_{15}\text{F}$ -wired  $\text{H-Nb}_2\text{O}_5$  at a scan rate of 1 mV/s with capacitive currents ( $k_1v$ ) outlined into orange area based on  $i(V) = k_1v + k_2v^{1/2}$ . Column graphs of rate-dependent charge storage contributions from both capacitive and intercalated processes for (e) pristine  $\text{Nb}_2\text{O}_5$  and (f)  $\text{KNb}_6\text{O}_{15}\text{F}$ -wired  $\text{H-Nb}_2\text{O}_5$ .

# ToC figure

